

# MESO-SCALE MODELLING OF SHOCK WAVE PROPAGATION IN A CELLULAR GLASS PARTICLE REINFORCED THERMOPLASTIC COMPOSITE

K.A. Brown\*, R. Brooks and O. Awoyemi  
 Division of Materials, Mechanics and Structures  
 Faculty of Engineering, University of Nottingham  
 University Park, Nottingham, NG7 2RD, United Kingdom  
 \*Corresponding author ([kevin.brown@nottingham.ac.uk](mailto:kevin.brown@nottingham.ac.uk))

**Keywords:** *multi-scale modeling, shock wave, particulate composite, finite element analysis*

## 1 Introduction

There is increasing interest in developing novel cellular particulate composite materials for shock mitigation and high energy absorbing applications in the defense and automotive industries [1]. However, such materials have high heterogeneous microstructures and their behavior under dynamic loading is complex. The aim of this study is to develop a comprehensive multi-scale modeling approach that accurately represents and simulates the real microstructure, morphology and behaviour of a new cellular particle reinforced thermoplastic composite under shock loading. A two-dimensional (2D) meso-scale statistical volume element (SVE) model of the material microstructure is generated. Numerical simulations are performed using the LS-DYNA explicit finite element code. The influence of volume fraction (vf), particle arrangement, and particle fracture on the mechanical response and shock wave attenuation of the material is investigated.

## 2 Material

The cellular particle reinforced thermoplastic composite developed in this study consists of near spherical cellular recycled glass particles ranging between 0.5 – 2 mm in diameter that are randomly distributed in a recycled foamed linear low density polyethylene (LLDPE) thermoplastic matrix (see Fig. 1). Composite panels were manufactured using a patented novel 'Layered Engineering Active Polymers' (LEAP) process developed by Crompton Mouldings Ltd, UK [2]. During fabrication, the cellular glass particulates, LLDPE powder and azodicarbonamide (AZO) blowing agent are mixed together before being fed into a preheated aluminum

mould. The composite is processed at approximately 200 °C for some 30 minutes before cooling at room temperature. Two types of particulate composites were manufactured, containing reinforcement volume fractions of 20% and 56%. These are referred to as LP20 and LP56, respectively. Both LP20 and LP56 have been experimentally characterized under dynamic compression loading at strain rates up to 6000/s using a split Hopkinson pressure bar (SHPB).

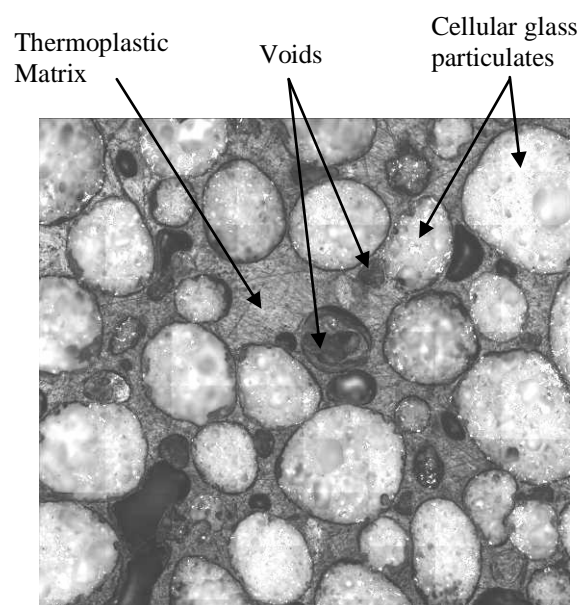


Fig. 1. Micrograph showing morphology of cellular glass particle composite microstructure, vf=20%.

## 3 Meso-scale Finite Element Model

As a first step in developing a meso-scale SVE finite element model, a 2D geometric model of the

material microstructure was auto-generated using the Digimat-FE software [3]. The generation process is based on the random placement of glass particles of a specified size range (0.5 - 2 mm diameter) and volume fraction into a matrix material domain 5mm x 5mm square. The cellular particles were represented as solid circles. The bond between particles and matrix was assumed to be perfect. The SVE mesh and boundary conditions are shown in Fig. 1. Embedded cell boundary conditions were applied whereby the heterogeneous SVE is embedded in a homogenous outer region that has the average properties of the composite material obtained from experimental tests, similar to the boundary conditions developed by Mishnaevsky [4]. The embedded approach avoids boundary effects on the SVE while accounting for the interaction between the SVE and the rest of the material. The embedding region was 10mm x 10mm square.

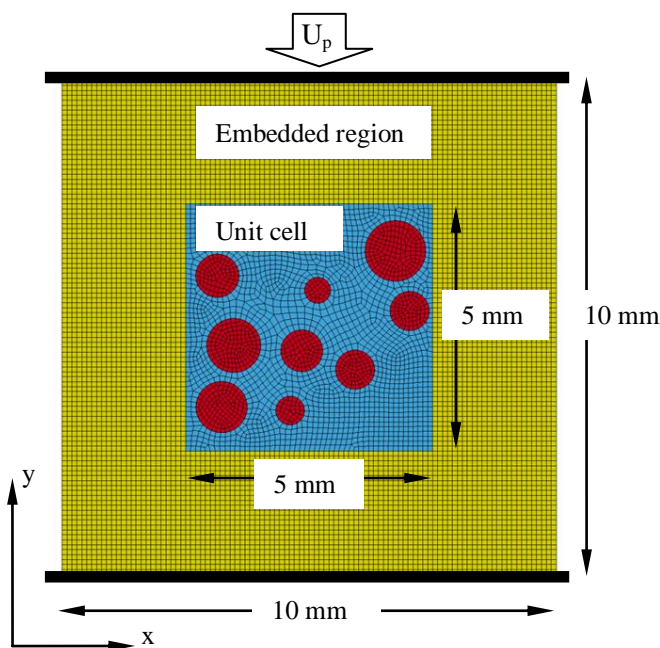


Fig. 1. Embedded SVE mesh and boundary conditions ( $\nu_f=20\%$ ).

Four-node plane-strain quadrilateral shell elements, with single integration points, were used to mesh the models. Following a mesh sensitivity study, elements with an average length of 0.1 mm were selected.

A compressive shock load was applied by imposing a specified initial velocity,  $U_p$ , along the y-axis to a rigid wall at the top of the embedded boundary. A fixed rigid wall is applied at the bottom of the embedded boundary.

The simulations were performed with the LS-DYNA explicit finite element code. Both the foamed thermoplastic matrix and the embedded boundary region were modeled with the LS-DYNA elastic-plastic foam material model, \*MAT\_CRUSHABLE\_FOAM [5]. The cellular glass particles were modeled as solid glass particles with the Johnson-Holmquist elastic-plastic damage model which is implement in LS-DYNA as \*MAT\_JOHNSON\_HOLMQUIST\_CERAMICS [5].

The properties for the embedded boundary were obtained from experimental dynamic compression tests on the actual composite material at strain rates up to 6000/s using a split Hopkinson pressure bar (SHPB). However the properties for the composite constituents, i.e. the foamed LLDPE matrix and the cellular glass particles were not readily available. In order to determine the input parameters for the matrix and glass particles, a numerical inverse calibration method was undertaken where parameters were systematically obtained by correlating simulations with the corresponding test data. The input parameters are adjusted iteratively over several simulation runs until satisfactory correlation was obtained.

All simulations were conducted on a HP Z600 workstation with 8 CPU (2.4 GHz) and 16 Gb RAM.

## 4 Results and discussion

### 4.1 Effect of volume fraction

Fig. 2 shows the random particle arrangements for the LP20 and LP56 models that were used to investigate the effect of volume fraction on the composite strength and shock response. Fig. 3 shows a comparison of experimental and simulation compression stress-strain curves for LP20 and LP56. The composites were loaded to 60% strain. As shown in Fig. 3 there is good correlation between the simulation and experimental results. In general, the stress-strain response is similar to other conventional cellular solids (foams) exhibiting an initial elastic response followed by yielding and

plastic deformation. The yield strength and plastic flow stress increased with increasing volume fraction.

The average shock wave velocity ( $U_s$ ) was obtained by averaging the time of arrival of the stress wave across the SVE along the axial direction ( $y$ ) at 1 mm intervals. It was observed that the average shock wave velocity decreases with increasing particle volume fraction content. For LP20,  $U_s = 3849$  m/s while for LP56,  $U_s = 2401$  m/s, which is a 38% difference. The dramatic drop in the  $U_s$  at high volume fractions is due to the higher number of particles that are more closely packed together which result in significant dispersion of the shock wave compared to LP20.

Fig. 4 shows the stress wave propagation through LP20 and LP56 at different time intervals. The shock wave is characterized by a dispersed non-uniform shock front with stress fingers that flow around the particles ahead of the compaction wave. As the shock wave front approaches the bottom of the SVE one can observe the formation of stress bridges, with regions of high compressive stress between particles that are aligned with each other parallel to the shock wave direction. The formation of stress bridges has also been observed elsewhere for other granular materials under shock loading [6]. According to Borg [6] these stress bridges occur when the shock wave propagates without the development of release waves from free surfaces. Stress bridges result in high stress concentration zones between particles and lead to eventual particle collapse and failure as the material is compacted.

The average compression stress and hydrostatic pressure profiles for LP20 and LP56 at 3  $\mu$ s are shown in Fig. 5. These values were obtained by averaging the pressure and stress across the SVE along the axial direction ( $y$ ) at 0.2 mm intervals. It should be noted that such averaging results in the smoothing of the stress and pressure variability and the loss of substantial detail; however, the general features are still recognizably and allows for easier comparison of results for various SVE models. For both LP20 and LP56, relatively low pressures are observed behind the shock front (about 1 MPa). In addition, a rather gradual reduction in the amplitude of the pressure and compressive stress occurs at the shock front. This was due in part to the weak shock loading conditions where the particle velocity,  $U_p$

(impactor speed) is much less than the speed of sound in the sample [7].

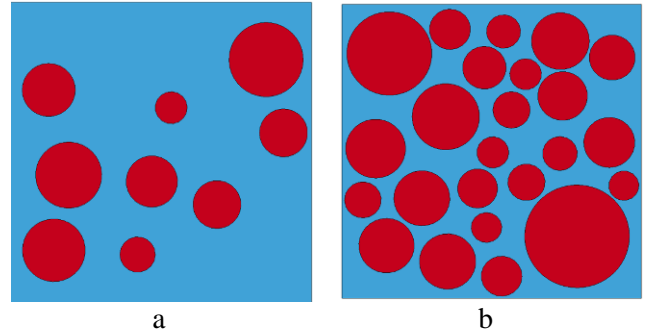


Fig. 2. Random particle arrangements for (a) LP20 and (b) LP56.

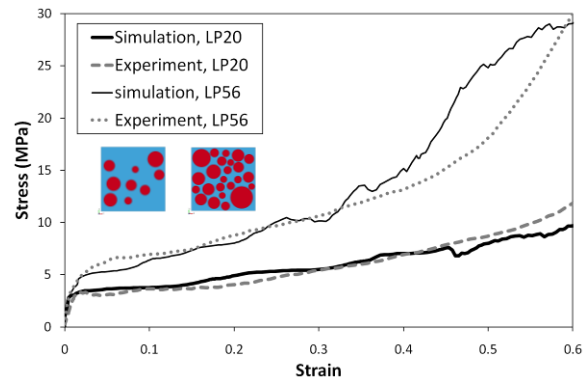


Fig. 3. Stress-strain curves for LP20 and LP56 at volume fractions 20% and 56%, respectively.

#### 4.2 Effect of particle arrangement

Firstly, the effect of various uniform random particle distributions with the same volume fraction was investigated. The various random particle arrangements with a volume fraction of 20% are shown in Fig. 6. One can see from Fig. 7 that the stress-strain response of the various particle arrangements is very similar for up to 60% strain. The small oscillations in the curves at 40% strain are due to the onset of damage in the balls. It is at this point that one can observe a very small divergence between the curves as the particle fracture pattern varies with the particle spatial arrangements in each model.

The maximum difference between the average shock wave velocities for the various random particle arrangements was insignificant at 3%. These results indicate that both the mechanical response and

average shock velocity show very little sensitivity to statistical variations in uniform random distributions of the same volume fraction.

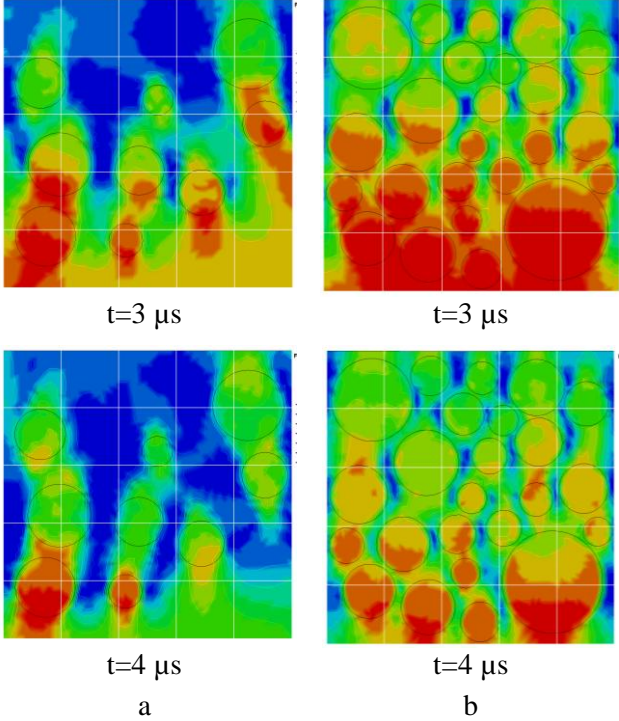


Fig. 4. Contour the stress wave propagation in (a) LP20 and (b) LP60. Dark contours represent the highest compressive stress regions.

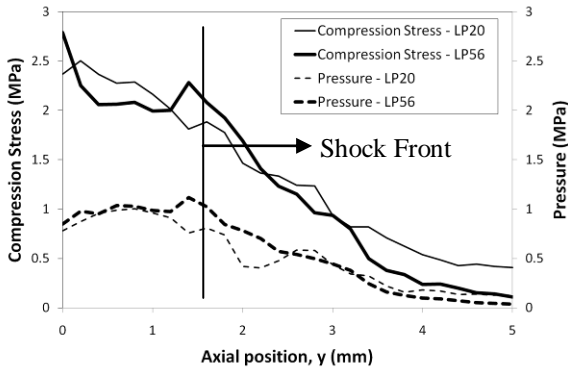


Fig. 5. Averaged compression stress and pressure profiles for LP20 and LP56 for  $t=3\mu s$ .

Three types of gradient (Grad-HT, Grad-HB and Grad-V) and one clustered particle arrangement, having the same volume fraction of 20%, were considered. Fig. 8 shows the particle arrangements for Grad-HT, Grad-HB and Grad-V having all particles concentrated at the top, bottom and to the right hand side, respectively.

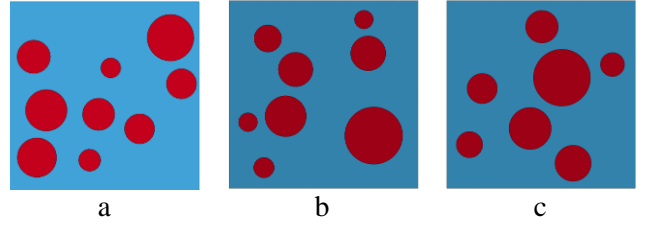


Fig. 6. Random particle arrangement for  $vf=20\%$ : (a) Random-1 (b) Random-2 and (c) Random-3.

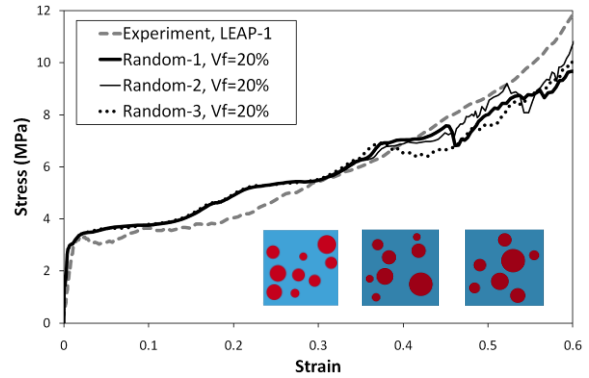


Fig. 7. Stress-strain curve for various uniform random particle distributions with  $vf=20\%$ .

The clustered arrangement has particles clustered diagonally opposite each other. Fig. 9 shows that the stress-strain response is not sensitive to the gradient and clustered particle arrangements up to 40% strain. There are only marginal deviations that occur after 40% strain which, again, is a result of the onset of particle damage. In addition, Grad-V exhibits a slightly stiffer response than the others after 40% strain.

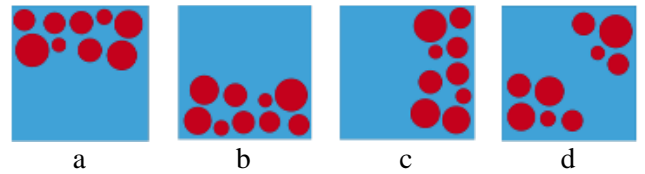


Fig. 8. Gradient (a) Grad-HT (b) Grad-HB (c) Grad-V and (d) clustered particle arrangements

The shock wave velocity,  $U_s$ , at 1 mm intervals along the SVE axial direction ( $y$ ) for these variants is shown in Fig. 10. The shock wave velocity for the random, clustered and Grad-V all exhibited a near constant shock speed along the SVE.

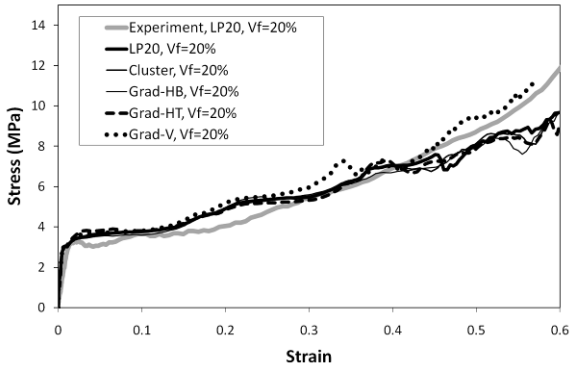


Fig. 9. Stress-strain curves for various particle arrangements with  $vf=20\%$ .

However, for Grad-HT, the high concentration of particles at the top of the SVE, which forms a high volume fraction zone, reduces the initial shock wave velocity after 1 mm to 2835 m/s; however, the shock velocity increases after entering the matrix only region reaching 3708 m/s at 5 mm, the bottom of the SVE. In contrast, for Grad-HB, the initial shock velocity in the matrix only region is 4987 m/s, which is 43% greater than initial shock velocity for Grad-HT and only reduces to 3708 m/s after passing through the particles at the bottom of the SVE. The low  $U_s$  for Grad-HT occurs because the shock wave is dispersed and slowed down by the particles at the top of the SVE. The shock wave is then further dampened by the matrix material before reaching the bottom of the SVE. On the other hand, for Grad-HB, a fast moving shock wave with a uniform shock front travels through the matrix material uninterrupted before being dispersed and slowed down when it enters the high concentration of particles at the bottom of the SVE.

The average shock wave velocity for the various particle arrangements is shown in Fig. 11. Grad-HB which has a high concentration of particles at the bottom of the SVE has the highest shock speed velocity, 4186 m/s. LP56, the highest  $vf\%$ , has the lowest average shock wave velocity, 2401 m/s. This is a significant 43% reduction. Grad-HT with the particles concentrated at the top of the SVE has the second lowest, 3246 m/s.

LP20 Grad-V, with particles concentrated to one side of the SVE, and the clustered arrangement exhibited shock wave velocities only marginally less than that for Grad-HB.

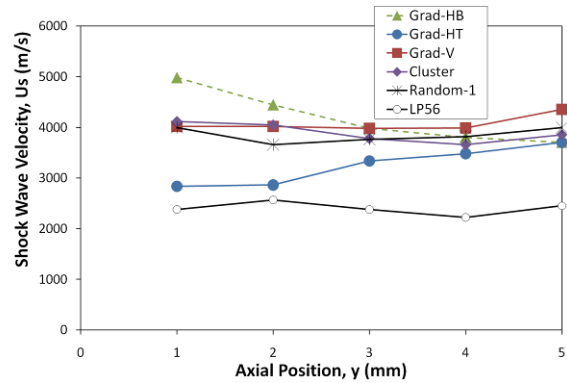


Fig. 10. Shock wave velocity along the axis of the SVE at 1 mm intervals for various particle arrangements.

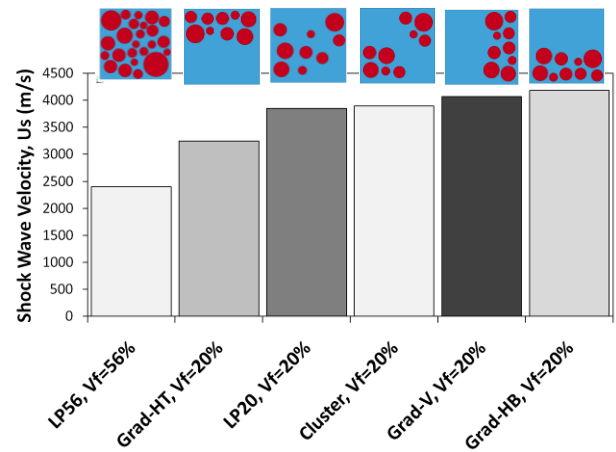


Fig. 11. Average shock wave velocity for various particle arrangements.

### 4.3 Damage morphology

The predicted glass particle deformation and failure of the LP56 models shows good agreement to micro computed tomography (microCT) scans taken after impact loading (see Fig. 12). As mentioned above, stress bridges cause stress concentrations and eventual particle failure. Typically, the particles exhibit severe plastic deformation and crush, becoming ellipsoidal before finally collapsing. This is a consequence of the internal cellular structure of the particles. As expected, more particles deform and fail at higher volume fractions and strain rates. Simulation results reveal failure occurs when a particle's circumferential tensile strength is reached, resulting in the propagation of diametric cracks parallel to the loading direction ( $y$ ).

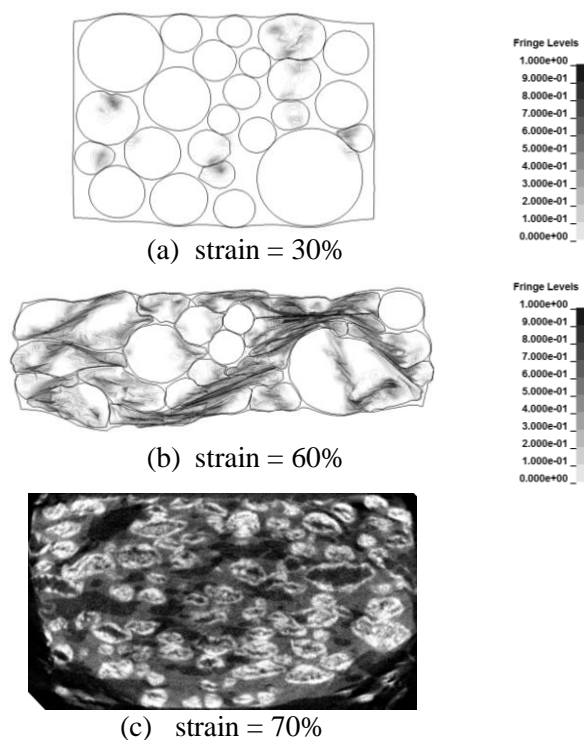


Fig. 12. Deformation morphology for LP56 (a) predicted particle deformation and damage at strain = 30% (b) predicted particle deformation and damage at strain = 60% and (c) microCT image of LP56 sample at 70% strain.

### Conclusion

The compressive shock load response of a cellular glass particle reinforced thermoplastic composite has been investigated through a meso-scale SVE finite element model. The following conclusions have been drawn:

1. The yield strength and plastic flow stress increase with increasing volume fraction
2. The shock wave velocity decreases with increased particle volume fraction content. This is due to the higher level of dispersion of the shock wave at high volume fractions.
3. The variations in the particle arrangement including uniformly random, gradient and clustered arrangements, has very little influence on the effective elastic-plastic material response up to 40% strain at  $\nu_f=20\%$ .
4. The shock wave velocity is influenced by the particle arrangement, with gradient arrangements of particles concentrated at the top of the SVE having a much lower shock wave

velocity than when the particles are concentrated at the bottom.

5. Of all the particle arrangements investigated in this study, the uniformly random, high volume fraction system, LP56, was most effective in attenuating the shock wave.

Future work will involve the use of the SVE model to fully optimize the material system for shock attenuation.

### Acknowledgements

This research is part of the SHIELD (Sustainable High Energy Absorbing Light Weight Material Development) project which is part funded by the EPSRC and the Technology Strategy Board (TSB) Collaborative Research and Development program. The TSB is an executive body established by the Government to drive innovation. It promotes and invests in research, development and the exploitation of science, technology and new ideas for the benefit of business. For more information visit: [www.innovateuk.org](http://www.innovateuk.org). The authors are grateful for the support received from industrial partners: AIGIS Blast Protection, MIRA, Crompton Mouldings, Archimedes Polymer Technologies (APT), EPL Composite Solutions and ThermoCOMP.

### References

1. Klaus, H., O. Huber, and G. Kuhn, *Lightweight potential of novel cellular spherical composites*. *Advanced Engineering Materials*, 2005. **7**(12): p. 1117-1124.
2. <http://www.cromptonmouldings.co.uk/>. [cited 2010 15 Feb.].
3. *e-Xstream Engineering*. Digimat Manual, 2009.
4. Mishnaevsky, L.L., *Three-dimensional numerical testing of microstructures of particle reinforced composites*. *Acta Materialia*, 2004. **52**(14): p. 4177-4188.
5. Hallquist, J.O., *LS-DYNA Keyword User's Manual Version 9712007*, Livermore: Livermore Software Technology Corporation.
6. Borg, J.P. and T.J. Vogler, *Mesoscale calculations of the dynamic behavior of a granular ceramic*. *International Journal of Solids and Structures*, 2008. **45**: p. 1676-1696.
7. Bardenhagen, S.G., *Dynamic stress bridging in granular material*. *Journal of Applied Physics*, 1998. **83**(1): p. 5732-5740.